International Journal of Pharmaceutics 395 (2010) 324–330

Contents lists available at ScienceDirect

International Journal of Pharmaceutics

journal homepage: www.elsevier.com/locate/ijpharm

Pharmaceutical Nanotechnology

In vivo PET imaging and biodistribution of radiolabeled gold nanoshells in rats with tumor xenografts

Huan Xie[a,*], Zheng Jim Wang[b,c], Ande Bao[b], Beth Goins[b], William T. Phillips[b]

[a] Department of Pharmaceutical Sciences, College of Pharmacy and Health Sciences, Texas Southern University, 3100 Cleburn St., Houston, TX 77004, United States
[b] Department of Radiology, University of Texas Health Science Center at San Antonio (UTHSC-San Antonio), San Antonio, TX, United States
[c] MPI Research, Inc., Mattawan, MI, United States

ARTICLE INFO

Article history:
Received 16 February 2010
Received in revised form 20 May 2010
Accepted 1 June 2010
Available online 9 June 2010

Keywords:
Nanoshells
Copper-64
PET
Pharmacokinetics
Biodistribution
Cancer therapy

ABSTRACT

Here we report the radiolabeling of gold nanoshells (NSs) for PET imaging in rat tumor model. A conjugation method was developed to attach NSs with the radionuclide, ^{64}Cu. The resulting conjugates showed good labeling efficiency and stability in PBS and serum. The pharmacokinetics of ^{64}Cu-NS and the controls (^{64}Cu-DOTA and ^{64}Cu-DOTA-PEG2K) were determined in nude rats with a head and neck squamous cell carcinoma xenograft by radioactive counting. Using PET/CT imaging, we monitored the *in vivo* distribution of ^{64}Cu-NS and the controls in the tumor-bearing rats at various time points after their intravenous injection. PET images of the rats showed accumulation of ^{64}Cu-NSs in the tumors and other organs with significant difference from the controls. The organ biodistribution of rats at 46 h post-injection was analyzed by radioactive counting and compared between the ^{64}Cu-NS and the controls. Different clearance kinetics was indicated. Neutron activation analysis (NAA) of gold concentration was performed to quantify the amount of NSs in major tissues of the dosed rats and the results showed similar distribution. Overall, PET images with ^{64}Cu had good resolution and therefore can be further applied to guide photothermal treatment of cancer.

Published by Elsevier B.V.

1. Introduction

Nanostructures have been intensively studied and broadly utilized for biological applications, such as molecular imaging, molecular diagnosis and targeted therapy (Jain et al., 2008). Among newly developed nanostructures, gold nanoshells (NSs) are of special interest for cancer treatment because of their unique size, composition, physical and optical properties. NSs are spherical nanoparticles consisting of a dielectric core and a metal shell, where the plasmon resonance frequency is determined by the relative size of the core and the metal shell layer (Oldenberg et al., 1998). By adjusting the relative core and shell thicknesses, NSs can be fabricated that will absorb or scatter light across the visible and near-infrared regions of the electromagnetic spectrum. Silica core gold NSs are made of biocompatible materials and their surface can be modified with "stealthing" polymers like polyethylene glycol (PEG) to further improve their biocompatibility. They can also be manufactured with size ranges that can accumulate in tumors via the enhanced permeability and retention (EPR) effect (Maeda et al., 2001, 2003). NS-based photothermal ablation has been demonstrated to be effective in the elimination of solid tumors in animal models (Hirsch et al., 2003; O'Neal et al., 2004).

An understanding of the fate and biological effects of nanoparticles in animals is critical to their application *in vivo*. Pharmacokinetic and organ/tissue distribution properties of NSs are of great interest from the clinical point of view because of the potential for cancer imaging and therapy. Systematic studies are required to evaluate the distribution of administrated NSs inside the body, especially at the tumor site, over time after injection. However, there have been few prior reports on the biodistribution of NSs, whereas the *in vivo* biodistributions of other popular nanomaterials have been reported. The biodistribution and tumor targeting ability of copper-64 and indium-111 labeled carbon nanotubes has been investigated in rats and mice by *in vivo* positron emission tomography (PET) and single photon emission computed tomography (SPECT) (Liu et al., 2007; Lacerda et al., 2008). McDevitt et al. (2007) also studied the tissue biodistribution and pharmacokinetics of prototypical DOTA-functionalized carbon nanotubes labeled with yttrium-86 and indium-111 in a mouse model by PET imaging. Cai et al. (2006) reported the *in vivo* targeting and imaging of tumor vasculature using RGD peptide-quantum dot conjugates. Terentyuk et al. (2009) studied the circulation and distribution of several different gold nanoparticles (colloids and NSs) with atomic absorption spectroscopy.

In this paper we report a new procedure for labeling gold NSs with the radionuclide, ^{64}Cu, and the biodistribution of the radiolabeled NSs in live rats bearing head and neck squamous cell carcinoma (HNSCC) xenografts by PET imaging. Classical biodis-

* Corresponding author. Tel.: +1 7133134340; fax: +1 7133134219.
E-mail address: xieh@tsu.edu (H. Xie).

0378-5173/$ – see front matter. Published by Elsevier B.V.
doi:10.1016/j.ijpharm.2010.06.005

tribution studies that quantify radiolabeled particle deposition provide results in terms of populational averages at specific time points, but do not allow particle localization to be monitored longitudinally in individual animals. PET is a noninvasive imaging tool that allows researchers to quantitatively image the uptake of candidate nanoparticles at the target site with high sensitivity in real time. Since the efficacy of photothermal therapy is mostly contributed by the potency of nanoparticle absorption in tumors, PET imaging is very helpful for NS-based photothermal ablation. In addition to conventional *ex vivo* biodistribution techniques, the pharmacokinetic profile of new nanomaterials with potential medical applications can be obtained with PET studies on a relatively small number of laboratory animals (Wipke et al., 2002). We systematically investigated the pharmacokinetics and the *in vivo* distribution of ^{64}Cu-NS and compared with the control radiolabeling intermediates (^{64}Cu-DOTA and ^{64}Cu-DOTA-PEG2K).

2. Materials and methods

2.1. Radiolabeling of NSs and stability test

Gold NSs were synthesized as previously described (Oldenburg et al., 1999). NSs formation was assessed using a UV–vis spectrophotometer (U-0080D, Hitachi, Schaumburg, IL) and Zetasizer (Nano-ZS, Malvern, Westborough, MA). NSs manufactured in this manner have an 8–10 nm gold shell around a 110–120 nm silica sphere.

The labeling process is shown in Fig. 1. First, a bifunctional chelating agent p-NH_2-Bn-DOTA (S-2-(4-aminobenzyl)-1,4,7,10-tetraazacyclododecane tetraacetic acid) (Macrocyclics, Dallas, TX) was conjugated to bifunctional OPSS-PEG2K-NHS (opyridyldisulfide-polyethylene glycol 2000-N-hydroxy-succinimide ester) (Nektar, Huntsville, AL). p-NH_2-Bn-DOTA and OPSS-PEG2K-NHS were mixed in a 1:1 molar ratio and the mixture incubated overnight at RT. The resulting OPSS-PEG-DOTA was then added to NS solution (in 10 mM phosphate buffer, pH 7) at 10,000:1 molar ratio followed by overnight incubation at RT on a shaker, allowing the OPSS group to conjugate to the gold surface of the particles. The mixture was centrifuged and the supernatant with unconjugated OPSS-PEG-DOTA was removed. The pellets of DOTA-NS were re-suspended in phosphate buffer and checked with spectrophotometer and Zetasizer to determine the NS concentration and size for further conjugation.

All the radioactive research was performed in the Department of Radiology, UTHSC-San Antonio. $^{64}CuCl_2$ (Washington University, St. Louis, MO) was diluted in 30 mM ammonium citrate buffer (pH 6.5). Then 213 MBq (5.76 mCi) of ^{64}Cu was added to 450 μL of the DOTA-NS solution (~0.8 nM) prepared as described above and incubated at 37 °C for 90 min followed by the addition of blocking agent PEG5K-SH (Nektar, Huntsville, AL) in 300,000:1 molar ratio and incubation at RT on a shaker for 1 h. The mixtures were then centrifuged to remove unconjugated $^{64}CuCl_2$ and PEG5K. The ^{64}Cu-activity of the supernatant and pellet was measured in dose calibrator (Atomlab 100, Biodex, Shirley, NY). Labeling efficiencies were calculated by using the relation: [activity in pellet/(activity in supernatant + activity in pellet)] × 100.

The radiolabel stability was investigated by incubating ^{64}Cu-NS in PBS and serum at 37 °C for up to 3 h. Suspensions were divided into aliquots and at each time point one aliquot was centrifuged. The supernatants and pellets were collected for radioactive counting. Percentages of ^{64}Cu remaining on the NS were calculated by using the relation: [activity in pellet/(activity in supernatant + activity in pellet)] × 100.

The control sample of ^{64}Cu-DOTA was prepared by mixing 74 MBq (2.0 mCi) of $^{64}CuCl_2$ with 200 μL of 0.20 mM DOTA solution (pH 6.5) and incubating at 37 °C for 90 min. The ^{64}Cu-DOTA-PEG2K was prepared by mixing 74 MBq (2.0 mCi) of $^{64}CuCl_2$ with 200 μL of 0.20 mM DOTA-PEG2K solution (pH 6.5) and incubating at 37 °C for 90 min. Formation of ^{64}Cu complexes was verified by radio-thin layer chromatography using a mobile phase consisting of 50:50 MeOH/10% ammonium acetate on silica plates.

2.2. Animal model and PET imaging

A human HNSCC xenograft model in nude rats was established via subcutaneous inoculation of a HNSCC cell line, SCC-4 (Bao et al., 2006). Animal experiments with radioactive agents were

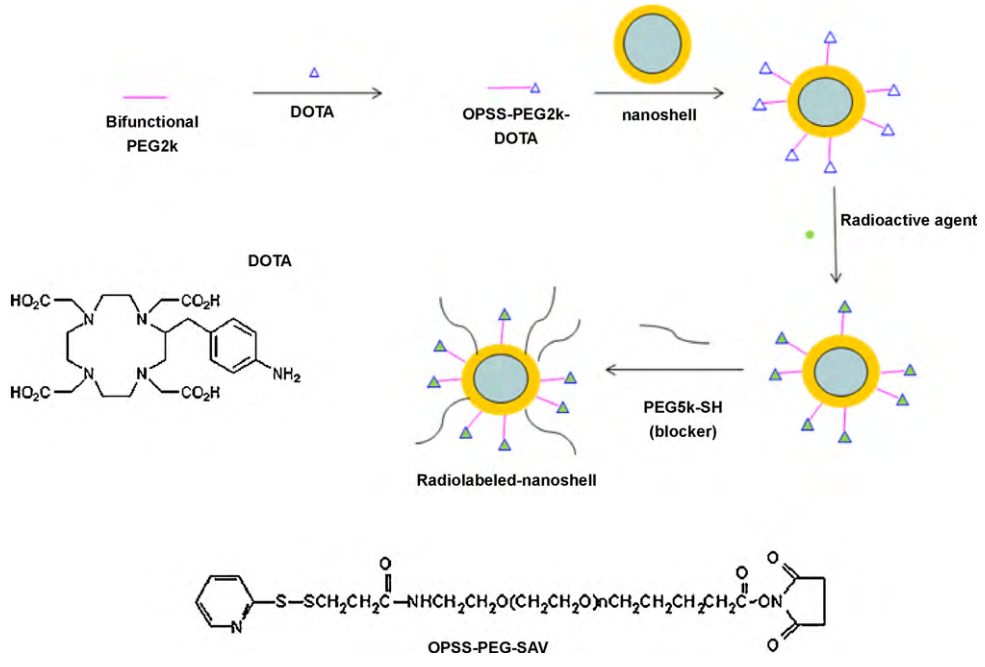

Fig. 1. Preparation of radiolabeled NSs.

performed at UTHSC-San Antonio according to the NIH Animal Use guidelines and Institutional Animal Care and Use Committee approval. On the day of imaging, the average weight of the rats was about 150 g and the average tumor volume was 385 mm^3, respectively. During all procedures, the nude rats were anesthetized with Avertin (400 mg/kg) by IP injections. There were four animals per group for ^{64}Cu-NS and three animals per group for the controls. ^{64}Cu-NS, ^{64}Cu-DOTA or ^{64}Cu-DOTA-PEG2K (0.5 ml; 17–18 MBq (460–490 μCi) of ^{64}Cu-activity) was injected into each rat at the tail vein. PET imaging was performed at 1, 4, 20 and 44 h post-injection (p.i.) with the FLEX X-PET/CT/SPECT (Gamma Medica-Ideas, Inc., Northridge, CA) followed by CT image acquisition (80 kVp, 0.25 mA, 256 projections).

2.3. Pharmacokinetics and biodistribution studies

Blood samples (40 μL) were collected from the opposite tail vein from the injection at 1, 4, 20, and 44 h p.i. time points. The ^{64}Cu radioactivity in blood samples were measured by a γ-counter (Wallac 1480, Perkin Elmer Life Sciences, Boston, MA).

The data are presented as the mean value with standard deviation from each group. SigmaPlot 10.0 (SYSTAT Software, Inc., San Jose, CA) was used for obtaining the curve fitting of pharmacokinetics data.

All the animals that were used in the imaging studies were anesthetized and then sacrificed at 46 h p.i. The organs of interest were removed and wet weighed. The radioactivity in the tissues was measured using a γ-counter. The radioactivity of the tissue samples was calibrated against a known aliquot of the injectate. The percent injected dose per gram of tissue (%ID/g) values were calculated using the following equation:

$$\%\frac{\mathrm{ID}}{\mathrm{g}} = \frac{(\text{cpm in sample} - \text{background}) \times 100}{(\text{tissue weight}) \times (\text{cpm in standard}) \times (\text{injection volume/standard volume})}$$

The percent injected dose per organ (%ID/organ) values were calculated using the following equation:

$$\%\frac{\mathrm{ID}}{\mathrm{organ}} = \frac{(\text{cpm in sample} - \text{background}) \times (\text{correction factor}) \times 100}{(\text{cpm in standard}) \times (\text{injection volume/standard volume})}$$

The total activities in bone, muscle and skin were calculated assuming 10%, 40% and 13% of the rat body weight, respectively (Frank, 1976; Petty, 1982).

2.4. Neutron activation analysis (NAA)

Some major organs from the biodistribution study were also subjected to NAA. Portions of spleen, liver, lung, kidney and tumor tissues were collected, wet weighed and allowed to decay for two weeks. The samples were placed into precleaned and labeled polyethylene irradiation vials. After the wet sample weight was calculated and recorded, the samples were covered and dried under a heat lamp for 48 h before delivery into the high temperature nuclear reactor core for NAA gold measurements. The procedure of NAA for trace gold quantification in animal tissues was described elsewhere (James et al., 2007). The data were reported as gold mass vs. the original wet sample mass.

2.5. Statistical analysis

One-way analysis of variance (ANOVA) and post hoc multiple comparison (Bonferroni's *t*-test) on the pharmacokinetics and biodistribution data (%ID/g and %ID/organ) were performed using SYSTAT 12 (SYSTAT Software, Inc., San Jose, CA), p values < 0.05 were considered statistically significant.

3. Results and discussion

3.1. Radiolabeling of NSs

NSs used in this study were manufactured to be comprised of a silica core (~120 nm in diameter) and a gold shell (8–10 nm) to absorb light at the near-infrared region. The UV–vis spectrum showed the NS peak at ~760 nm. Zetasizer measurements showed the NS size was around 140 nm in diameter and zeta potential was around −50 mV. The gold shell layer is formed using the same chemical methods that are employed to form gold colloid which has been proven to be inert (Hayat, 1989); thus, the surface properties of NSs are virtually identical to gold colloid, providing the same ease of bioconjugation and excellent biocompatibility.

A conjugation procedure was developed to label NS with ^{64}Cu ($t_{1/2}$ = 12.7 h), using bifunctional OPSS-PEG2K-NHS and bifunctional chelating agent DOTA-NH_2 (Fig. 1). First, OPSS-PEG2K-NHS and DOTA-NH_2 were mixed, and the NHS ester reacted with the amine group to form an amide bond. The mixture was then added to a NS solution allowing the OPSS group to attach to the gold surface of the particles. NSs were then coupled with $^{64}CuCl_2$ through DOTA.

Finally, the longer PEG5K-thiol was added to block the remaining empty areas on the gold surface to provide better PEG coverage. Zetasizer measurements showed that after surface modification, the NS size increased to about 170 nm in diameter and zeta potential was around −5 mV.

This conjugation chemistry has been broadly applied to attach different molecules to the NSs, such as antibodies (Loo et al., 2005; Lowery et al., 2006). We adapted this method to prepare PEGylated DOTA-NSs and found the conjugates were as stable as PEGylated NSs without DOTA in blood circulation (Xie et al., 2007) (see Supporting Information SI-1).

The radioactively labeled particles were thoroughly washed twice by centrifugation and re-suspension in fresh PBS buffer. The radioactive signal from both the pellet and the supernatant was measured in the dose calibrator to obtain the labeling efficiency, which is the radioactivity in the pellet vs. the total radioactive count. The average radiolabeling efficiency (n = 3) was 81.3% for ^{64}Cu-NS respectively after 2 separations.

Prior to any *in vivo* examination of ^{64}Cu-NS, *in vitro* stabilities in PBS and serum were tested. The labeled particles were incubated with either PBS or serum for 3 h, and then the samples were centrifuged and the supernatant removed. The radioisotope content of both the pellet and supernatant was determined by dose calibrator. The percentages of ^{64}Cu remaining on the particles after 3 h incubation with PBS and serum were both >90%.

NSs have been used to detect and destroy SKBr3 cancer cells, and showed good photothermal therapy potential (Loo et al., 2005; Lowery et al., 2006). Photothermal ablation of solid tumors in immune-competent mice using near-infrared illumination has also been conducted and complete regression of tumors in the NS-treated mice was observed (Hirsch et al., 2003; O'Neal et al., 2004). NSs are currently being evaluated in a human pilot study in refractory head and neck cancer under an approved Investigational Device Exemption (IDE). In connection with the IDE filing, the GLP preclinical and laboratory studies did not determine any systemic toxicity associated with infusion of the particles into the blood stream. Based on these evidences it can be concluded that NSs are biocompatible and non-toxic. Our NS conjugates have been modified with DOTA and only trace amount of ^{64}Cu. DOTA is well

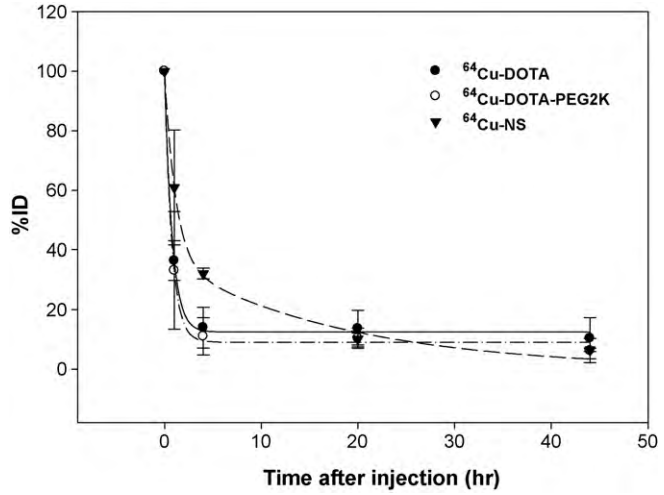

Fig. 2. Pharmacokinetics, expressed as the percentage of the injected dose (%ID), of ^{64}Cu-DOTA, ^{64}Cu-DOTA-PEG2K and ^{64}Cu-NS at 0, 4, 20 and 44 h p.i. The lines are curves fitted to exponential decay models. Significant difference between ^{64}Cu-NS and the two controls is evident at 4 h p.i. ($p < 0.05$).

recognized in the imaging literature to be biocompatible and some DOTA labeled products are available clinically (Milenic et al., 2004; De Leon-Rodriguez and Kovacs, 2008; Shokeen and Anderson, 2009). So we considered our NS conjugates to be biocompatible. The purpose of this study was to monitor NSs biodistribution *in vivo* so that we can better understand the clearance of NSs; determine the appropriate timing to apply laser treatment and have PET imaging to guide the thermal therapy. Therefore, we further applied the biocompatible ^{64}Cu-NSs for *in vivo* studies.

3.2. Animal model and pharmacokinetics studies

Because the *in vitro* studies showed successful radiolabeling of NSs, we proceeded to test ^{64}Cu-NS in tumor-bearing rats at UTHSC-San Antonio. Squamous cell carcinoma (SCC) is the most common type of head and neck cancer. A unique model of human HNSCC xenografts in nude rats has been successfully developed through subcutaneous administration of an established human-origin HNSCC tumor cell line, SCC-4 (Bao et al., 2006). Previous studies have shown that this tumor xenograft model has good reproducibility and 100% take rate in more than 40 nude rats. Nude rats rather than nude mice were chosen for this tumor xenograft model due to their larger body size, which permits a better organ differentiation in PET and a lower whole-body radiation dose. Therefore, PET/CT imaging and pharmacokinetics studies at multiple time points after injection of ^{64}Cu-NSs were performed in nude rats with HNSCC tumor xenografts model.

Blood samples were also collected at 1, 4, 20 and 44 h p.i. for radioactive counting. The simulated exponential decay circulation curves were obtained for ^{64}Cu-DOTA, ^{64}Cu-DOTA-PEG2K (controls) and ^{64}Cu-NS based on the average percentage of activity remaining in the blood samples from rats in each group (three rats per group for the two controls and four rats per group for ^{64}Cu-NS) at those time points (Fig. 2). The retention of ^{64}Cu-DOTA and ^{64}Cu-DOTA-PEG2K in the rat blood followed a 3-parameter exponential decay model and ^{64}Cu-NS followed a 4-parameter exponential decay model. The data revealed that the half lives for ^{64}Cu-DOTA, ^{64}Cu-DOTA-PEG2K and ^{64}Cu-NS were 0.54, 0.52 and 12.76 h. Statistical analysis revealed that ^{64}Cu-NS had much higher percentage remaining in the blood at 4 h p.i. than the two controls (32.1 ± 1.8%ID vs. 13.9 ± 6.8 and 11.0 ± 6.2; $p < 0.05$). The results clearly showed different pharmacokinetics when ^{64}Cu is attached to the NSs. Also the prolonged half life of ^{64}Cu-NS revealed that the ^{64}Cu radiolabel remained attached to NSs *in vivo*.

For intravenous injection, nanoparticles are required to have reasonable stability in circulation and to avoid recognition by the reticuloendothelial system (RES), which rapidly recognize and ingest most injected nanoparticles as foreign substances. Surface characteristics and size of nanoparticles both play important roles in the blood clearance kinetics (Moghimi et al., 2005). Modification of the surface of nanoparticles by a stealth polymer such as PEG is a useful method to greatly reduce RES uptake. It is known that RES uptake of nanomaterials is size-dependent and should be higher for larger sizes. Larger particles (200 nm and above) are generally cleared faster from the blood by the liver (Kupffer cells). Zhang et al. reported that ^{111}In-labeled PEG5000-thioctic acid-coated gold nanospheres with diameter of 20, 40 and 80 nm had average blood clearance half lives in mice of 22.5, 10.1 and 15.8 h, respectively. They claimed that the 20 and 40-nm gold nanospheres were cleared from the blood more slowly and had less uptake in the liver and spleen than the 80-nm particles (Zhang et al., 2009). Liu et al. showed that single-walled carbon nanotubes (diameter ~1–5 nm, length ~100–300 nm) with PEG5400 coverage had a half life of 2 h in mice whereas with PEG2000 coverage the half life was only 0.5 h (Liu et al., 2007). von Maltzahn et al. (2009) reported that their PEG5000-gold nanorods (~13 nm × 47 nm) had a 17 h of blood circulation half life in mice. Akiyama et al. also studied gold nanorod circulation with different amounts of surface coverage of PEG5000 and different particle injection amounts. They showed the pharmacokinetics plots, but did not provide the half life data (Akiyama et al., 2009). Our NSs were coated with PEG5000 and the dynamic light scattering studies showed that the diameter of NSs changed from ~140 to ~170 nm and the zeta potential changed from −50 to −5 mV after conjugation with PEG. Those changes confirmed the coverage of PEG on the surface of the particles. The naked NSs were found to be cleared within minutes from blood after intravenous injection by a dynamic light scattering method developed in house (Xie et al., 2007). The PEG-NSs had an average blood clearance half life of 12.76 h in the tumor-bearing rats, which is similar to gold nanospheres and gold nanorods with smaller sizes, and is much longer than single-walled carbon nanotubes of the similar size. Considering the size of our NSs, the half life is high among the inorganic nanomaterials.

3.3. Biodistribution studies

Using PET/CT imaging, we monitored the *in vivo* distribution at various time points after intravenous injection of ^{64}Cu-NS and the two controls in nude rats with a HNSCC xenograft. Fig. 3 shows the PET sagittal images of three rats at 1, 4, 20 and 44 h after injection of controls, ^{64}Cu-DOTA and ^{64}Cu-DOTA-PEG2K, and ^{64}Cu-NS as well as the corresponding CT images denoting the location of the tumor in each rat. As we can see, the two controls had some weak tumor accumulation starting from 1 h after injection which did not increase over time. The low tumor uptake by the controls was most likely due to the rapid clearance of the controls from the blood pool as noted by little uptake in the heart at 1 and 4 h p.i. as well as rapid uptake in the liver and kidneys. In contrast, ^{64}Cu-NS tumor accumulation at 1 h p.i. was not significant, but increased over time. At 20 h p.i. tumor accumulation achieved a plateau, and at 44 h, the majority of accumulated particles were still at the tumor site. This increased tumor uptake was due to a slower removal of ^{64}Cu-NS from the blood pool as denoted by heart activity on the 1 and 4 h images and the pharmacokinetic data depicted in Fig. 2. Although the radioactivity accumulation in the liver and spleen was quite high, the tumor was still clearly visualized with good tumor-to-contralateral background contrast at 1–44 h p.i. These

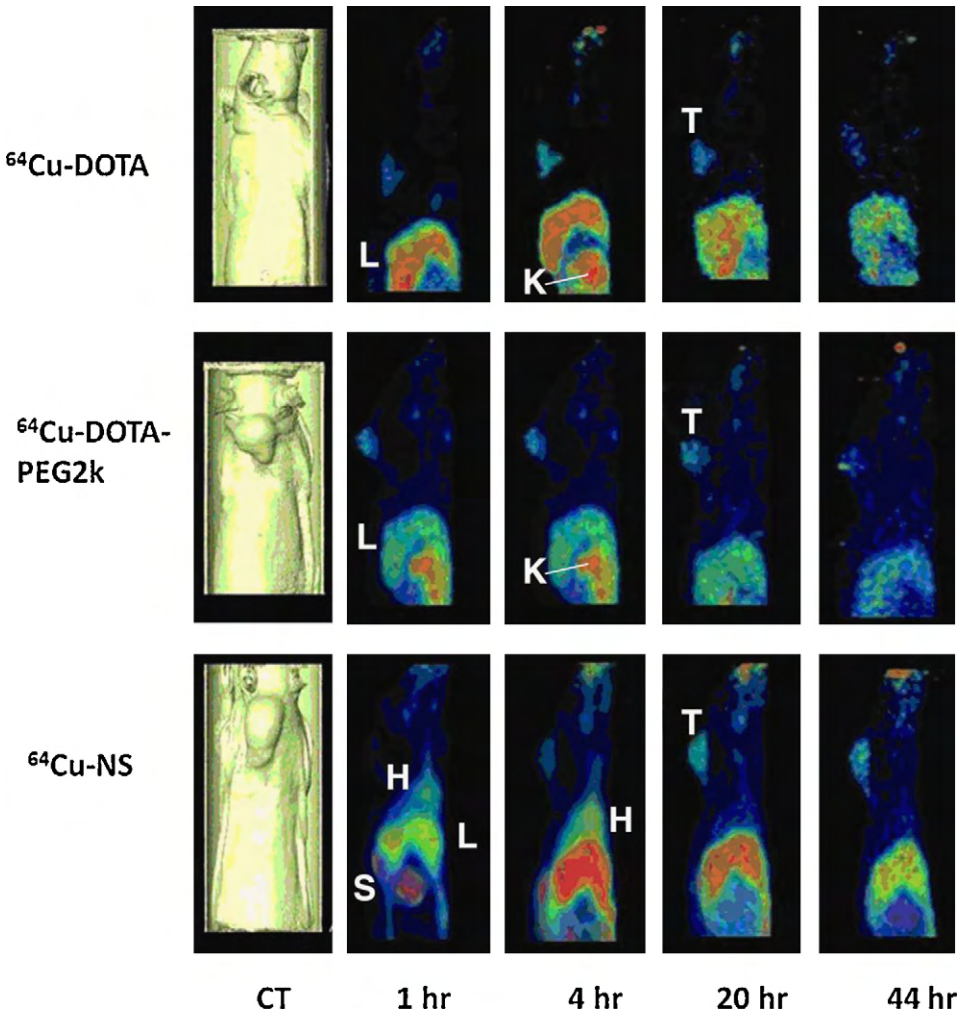

Fig. 3. Sagittal PET images of three rats acquired at various time points after tail vein injection of ^{64}Cu-DOTA, ^{64}Cu-DOTA-PEG2K and ^{64}Cu-NS, respectively. Surface rendered CT images depicting tumor location are also shown (H, Heart; L, Liver; S, Spleen; K, Kidneys; T, Tumor). Color intensity scale is denoted as red > yellow > green > blue.

Table 1
Biodistribution data of ^{64}Cu-DOTA, ^{64}Cu-DOTA-PEG2K and ^{64}Cu-NS in HNSCC xenograft-bearing nude rats (n = 3, 3, 4) at 46 h p.i.

Organ	^{64}Cu-DOTA		^{64}Cu-DOTA-PEG2K		^{64}Cu-NS	
	%ID/g	%ID/organ	%ID/g	%ID/organ	%ID/g	%ID/organ
Tumor	0.15 ± 0.09	0.18 ± 0.09	0.09 ± 0.02	0.17 ± 0.07	0.77 ± 0.09**	0.97 ± 0.11**
Spleen	0.06 ± 0.05	0.04 ± 0.00	0.05 ± 0.00	0.06 ± 0.00	14.51 ± 1.35**	4.93 ± 0.20**
Liver	0.33 ± 0.24	2.11 ± 0.70	0.36 ± 0.02	2.96 ± 0.14	1.93 ± 0.20**	16.39 ± 1.92**
Lung	0.06 ± 0.05	0.08 ± 0.03	0.04 ± 0.00	0.07 ± 0.01	0.33 ± 0.05**	0.31 ± 0.07**
Kidney	0.35 ± 0.18	0.66 ± 0.09	0.39 ± 0.02	0.97 ± 0.12	1.08 ± 0.15**	1.76 ± 0.15**
Blood	0.06 ± 0.04	0.40 ± 0.18	0.07 ± 0.02	0.54 ± 0.21	0.27 ± 0.06**	2.26 ± 0.49**
Skin	0.05 ± 0.04	0.81 ± 0.57	0.03 ± 0.00	0.57 ± 0.14	0.24 ± 0.04**	4.80 ± 0.72**
Muscle	0.02 ± 0.02	1.18 ± 0.77	0.02 ± 0.00	1.06 ± 0.02	0.11 ± 0.02**	6.80 ± 0.90**
Bone	0.04 ± 0.02	0.45 ± 0.26	0.03 ± 0.00	0.45 ± 0.11	0.40 ± 0.01**	6.02 ± 0.09**
Heart	0.06 ± 0.05	0.05 ± 0.01	0.05 ± 0.00	0.07 ± 0.00	0.32 ± 0.03**	0.17 ± 0.01**
Stomach	0.06 ± 0.03	0.21 ± 0.13	0.03 ± 0.01	0.12 ± 0.03	0.29 ± 0.13*	0.76 ± 0.19**
Intestine	0.17 ± 0.12	1.28 ± 0.45	0.14 ± 0.03	1.36 ± 0.08	0.61 ± 0.10**	5.21 ± 0.48**
Cecum	0.20 ± 0.17	0.75 ± 0.30	0.14 ± 0.02	0.78 ± 0.13	0.51 ± 0.10*	3.16 ± 0.25**
Bladder	0.03 ± 0.01	0.01 ± 0.00	0.03 ± 0.01	0.02 ± 0.00	0.20 ± 0.05**	0.02 ± 0.02
Testis	0.04 ± 0.03	0.11 ± 0.05	0.04 ± 0.00	0.16 ± 0.02	0.28 ± 0.03**	0.62 ± 0.05**
Brain	0.01 ± 0.00	0.02 ± 0.00	0.01 ± 0.00	0.02 ± 0.00	0.04 ± 0.00**	0.06 ± 0.01**
Urine 0–20 h	7.2 ± 5.0	25.8 ± 11.4	8.2 ± 5.7	33.7 ± 21.0	0.63 ± 0.51	1.73 ± 1.21
Urine 20–46 h	0.92 ± 0.70	0.49 ± 0.39	0.20 ± 0.01	0.90 ± 0.08	0.57 ± 0.50	1.38 ± 1.00
Feces	2.11 ± 0.47	14.76 ± 2.61	1.93 ± 0.24	10.12 ± 1.50	2.90 ± 0.83	13.90 ± 3.42

Data are presented as percentage injected dose per gram of tissue (%ID/g) and percentage injected dose per organ (% ID/organ) ± SD.
* $p < 0.05$.
** $p < 0.01$.

results confirmed that the radioisotope distribution truly reflected the NSs distribution because it was quite different from the two other controls.

The rats were sacrificed at 46 h p.i., and major organs were collected. The amount of ^{64}Cu-NS in the tissue samples was quantified by gamma well counter and later by NAA. The percentages of injected dose per g of tissue and per organ were calculated and shown in Table 1. Statistical analysis was performed to compare differences in tissue uptake between the two controls and ^{64}Cu-NS. As we can see, the accumulations of ^{64}Cu-NS in tumor, spleen, liver, lung and kidney were all significantly different than those of the two controls ($p < 0.01$). For ^{64}Cu-NS, the highest %IDs were localized to RES organs of liver and spleen. The ^{64}Cu-NSs were rapidly taken up by the spleen and liver and then slowly cleared through the intestine as evident from 13.9% ID in feces at 46 h p.i. On the contrary, ^{64}Cu-DOTA and ^{64}Cu-DOTA-PEG2K were rapidly taken up by the liver and kidneys and then quickly eliminated as feces and urine. Urine samples collected from 0 to 20 h p.i. had much higher radioactivity in rats injected with ^{64}Cu-DOTA and ^{64}Cu-DOTA-PEG2K than in rats injected with ^{64}Cu-NSs (25.8%ID/organ and 33.7%ID/organ vs. 1.73%ID/organ). These results proved that the elimination of the two controls happened at an early stage (before 20 h p.i.) and confirmed that the radioisotope was not cleaved from the NSs, and the biodistribution data of ^{64}Cu-NS truly reflected the location of NSs.

Fig. 4 shows the biodistribution of NSs in several major organs, represented by gold concentration measured by NAA. After measuring the radioactivity counts, the selected tissue samples were allowed to decay prior to NAA. We also compared the radioactivity counts in each sample with the gold concentration (see Supporting Information SI-2). The two sets of data are highly correlated. This biodistribution data showed high accumulation in liver and spleen, consistent with the pharmacokinetics result and some previous reports on NSs (James et al., 2007; Terentyuk et al., 2009). The biodistribution of NSs was also similar to other reported nanomaterials with a tendency to undergo RES uptake (Zhang et al., 2009). As we discussed above, the size of the nanoparticles is an important factor for biodistribution. Nanoparticles larger than 200 nm were trapped by splenic physical filtration, while increased renal clearance was observed for nanoparticles smaller than 20 nm. NSs can passively accumulate in solid tumor due to the well-known EPR effect (Maeda et al., 2001, 2003). In this study, no targeting moiety was attached to the surface of NSs, so it was expected that the accumulation in tumor would be lower than the accumulation in liver and spleen, according to previous reports (Terentyuk et al., 2009; Zhang et al., 2009). The goal of this study was to monitor NSs localization and to guide the application of laser thermal therapy.

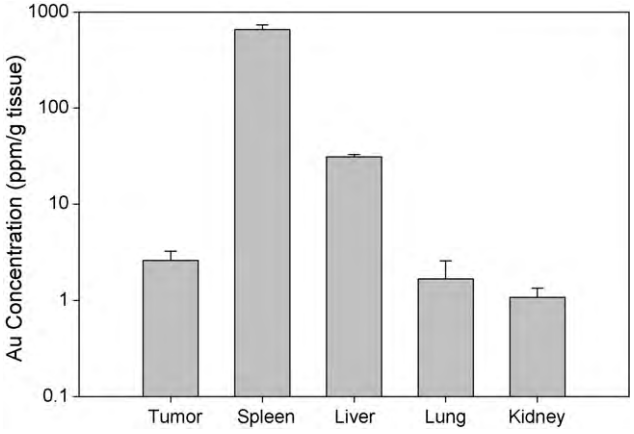

Fig. 4. Neutron activation analysis (NAA) of gold concentrations (representing NSs concentrations) in tumor, spleen, liver, lung and kidney at 46 h after injection of ^{64}Cu-NS.

Tumor levels revealed continual NSs accumulation until 20 h p.i. and most of NSs have been cleared from blood by then. Hence, this study suggests that optimal laser treatment should occur at around 20 h p.i.

4. Conclusion

PET images of the rats showed that ^{64}Cu appeared to be useful for tracking the *in vivo* distribution of NS, and ^{64}Cu-NS showed clear uptake in the tumor at 20 h after injection. This uptake is likely due to the well described EPR effect. PET image quality was better with the ^{64}Cu than in our studies with SPECT imaging with ^{111}In (Xie et al., 2010). This is likely due to the more efficient detection of the ^{64}Cu with the PET ring coincidence imaging system than the SPECT rotating camera system. Therefore, PET imaging with ^{64}Cu appears more promising for future NS imaging studies. Imaging provides the possibility not only of quantitative assessment of uptake in the tumor to ensure an adequate uptake for thermal therapy, but also can provide localization information to guide the application of photothermal therapy. PET imaging of ^{64}Cu-labeled NSs will be highly feasible for clinical patients.

Recently, small animal and clinical systems have become available that incorporate a CT scanner and a PET camera into the same housing (Rowland and Cherry, 2008). This permits superimposition of the PET and CT images so that the highly sensitive tracking and quantification of a PET radiolabeled agent can be localized with the higher anatomic accuracy of CT profile co-registrated with PET images. The very accurate localization provided by the CT imaging offers the possibility of effective image-guided application of photothermal ablation to specific locations of tumor in the body.

This study shows the feasibility of radiolabeling NSs for PET imaging using the procedures demonstrated in this article. This technique can be easily adapted for radiolabeling of other types of nanoparticles and radioactive agents. This radiolabeling procedure permits determination of *in vivo* biodistribution and tumor uptake of nanoparticles and offers optimum timing and guidance for laser thermal therapy. Further studies of the biodistribution of radiolabeled peptide-NS conjugates for the specific targeting of tumor neovasculature are under investigation now and we have already obtained promising preliminary results which also demonstrate the usefulness of PET imaging for investigation of different ^{64}Cu-labeled nanoparticle formulations.

Acknowledgments

This work was performed under funding from Nanospectra Biosciences, Inc. through NIST ATP Cooperative Agreement Number 70NANB4H3040. We thank Mr. J. Don Payne and Dr. Glenn Goodrich for the biocompatibility information. We also thank Dr. Ting Tung A. Chang for his imaging technical support.

Appendix A. Supplementary data

Supplementary data associated with this article can be found, in the online version, at doi:10.1016/j.ijpharm.2010.06.005.

References

Akiyama, Y., Mori, T., et al., 2009. The effects of PEG grafting level and injection dose on gold nanorod biodistribution in the tumor-bearing mice. J. Control. Release 139, 81–84.

Bao, A, Phillips, W.T., et al., 2006. Setup and characterization of a human head and neck squamous cell carcinoma xenograft model in nude rats. Otolaryngol. Head Neck Surg. 135, 853–857.

Cai, W., Shin, D.W., et al., 2006. Peptide-labeled near-infrared quantum dots for imaging tumor vasculature in living subjects. Nano Lett. 6, 669–676.

De Leon-Rodriguez, L.M, Kovacs, Z., 2008. The synthesis and chelation chemistry of DOTA-peptide conjugates. Bioconjug. Chem. 19, 391–402.

Frank, D., 1976. Physiological data of laboratory animals. In: Melby, E.J., Altman, N. (Eds.), Handbook of Laboratory Animal Science. CRC Press III, pp. 23–64.
Hayat, M., 1989. Colloidal Gold: Principles, Methods and Applications. Academic, San Diego.
Hirsch, L.R., Stafford, R.J., et al., 2003. Nanoshell-mediated near-infrared thermal therapy of tumors under magnetic resonance guidance. Proc. Natl. Acad. Sci. U.S.A. 100, 13549–13554.
Jain, P.K, Huang, X., et al., 2008. Noble metals on the nanoscale: optical and photothermal properties and some applications in imaging, sensing, biology, and medicine. Acc. Chem. Res. 41, 1578–1586.
James, W.D., Hirsch, L.R., et al., 2007. Application of INAA to the build-up and clearance of gold nanoshells in clinical studies in mice. J. Radioanal. Nucl. Chem. 271, 455–459.
Lacerda, L, Soundararajan, A., et al., 2008. Dynamic imaging of functionalized multiwalled carbon nanotube systemic circulation and urinary excretion. Adv. Mater. 20, 225–230.
Liu, Z., Cai, W., et al., 2007. In vivo biodistribution and highly efficient tumour targeting of carbon nanotubes in mice. Nat. Nanotechnol. 2, 47–52.
Loo, C, Lowery, A., et al., 2005. Immunotargeted nanoshells for integrated cancer imaging and therapy. Nano Lett. 5, 709–711.
Lowery, A.R., Gobin, A.M., et al., 2006. Immunonanoshells for targeted photothermal ablation of tumor cells. Int. J. Nanomed. 1, 149–154.
Maeda, H., Fang, J., et al., 2003. Vascular permeability enhancement in solid tumor: various factors, mechanisms involved and its implications. Int. Immunopharmacol. 3, 319–328.
Maeda, H, Sawa, T., et al., 2001. Mechanism of tumor-targeted delivery of macromolecular drugs, including the EPR effect in solid tumor and clinical overview of the prototype polymeric drug SMANCS. J. Control. Release 74, 47–61.
McDevitt, M.R., Chattopadhyay, D., et al., 2007. PET imaging of soluble yttrium-86-labeled carbon nanotubes in mice. PLoS One 2, e907.
Milenic, D.E, Brady, E.D., et al., 2004. Antibody-targeted radiation cancer therapy. Nat. Rev. Drug Discov. 3, 488–499.
Moghimi, S.M., Hunter, A.C., et al., 2005. Nanomedicine: current status and future prospects. FASEB J. 19, 311–330.
O'Neal, D.P, Hirsch, L.R., et al., 2004. Photo-thermal tumor ablation in mice using near infrared-absorbing nanoparticles. Cancer Lett. 209, 171–176.
Oldenberg, S.J., Averitt, R.D., et al., 1998. Nanoengineering of Optical Resonances. Chem. Phys. Lett. 28, 243–247.
Oldenburg, S.J., Jackson, J.B., et al., 1999. Infrared extinction properties of gold nanoshells. Appl. Phys. Lett. 111, 2897.
Petty, C., 1982. Research Techniques in the Rat. Springfield, IL.
Rowland, D.J., Cherry, S.R., 2008. Small-animal preclinical nuclear medicine instrumentation and methodology. Semin. Nucl. Med. 38, 209–222.
Shokeen, M, Anderson, C.J., 2009. Molecular imaging of cancer with copper-64 radiopharmaceuticals and positron emission tomography (PET). Acc. Chem. Res. 42, 832–841.
Terentyuk, G.S., Maslyakova, G.N., et al., 2009. Circulation and distribution of gold nanoparticles and induced alterations of tissue morphology at intravenous particle delivery. J. Biophotonics 2, 292–302.
von Maltzahn, G., Park, J.H., et al., 2009. Computationally guided photothermal tumor therapy using long-circulating gold nanorod antennas. Cancer Res. 69, 3892–3900.
Wipke, B.T., Wang, Z., et al., 2002. Dynamic visualization of a joint-specific autoimmune response through positron emission tomography. Nat. Immunol. 3, 366–372.
Xie, H., Gill-Sharp, K.L., et al., 2007. Quantitative estimation of gold nanoshell concentrations in whole blood using dynamic light scattering. Nanomedicine 3, 89–94.
Xie, H., Wang, Z., et al., 2010. Radiolabeled Gold Nanoshells for In Vivo Imaging: Example of Methodology for Initial Evaluation of Biodistribution of a Novel Nanoparticle Nanoimaging-Biomedical Nanotechnology. Pan Stanford Publishing Pte Ltd.
Zhang, G., Yang, Z., et al., 2009. Influence of anchoring ligands and particle size on the colloidal stability and in vivo biodistribution of polyethylene glycol-coated gold nanoparticles in tumor-xenografted mice. Biomaterials 30, 1928–1936.